15 May 2022

Engineering Metal-Oxide Interface by Depositing ZrO2 overcoating on Ni/Al2O3 for Dry Reforming of Methane

Baitang Jin

Shiguang Li

Yuzi Liu

Xinhua Liang
Missouri University of Science and Technology, liangxin@mst.edu

Recommended Citation

B. Jin et al., "Engineering Metal-Oxide Interface by Depositing ZrO2 overcoating on Ni/Al2O3 for Dry Reforming of Methane," *Chemical Engineering Journal*, vol. 436, article no. 135195, Elsevier, May 2022. The definitive version is available at https://doi.org/10.1016/j.cej.2022.135195

Chemical Engineering Journal 436 (2022) 135195

Contents lists available at ScienceDirect

Chemical Engineering Journal

journal homepage: www.elsevier.com/locate/cej

Engineering metal-oxide interface by depositing ZrO_2 overcoating on Ni/Al_2O_3 for dry reforming of methane

Baitang Jin [a], Shiguang Li [b], Yuzi Liu [c], Xinhua Liang [a,*]

[a] Linda and Bipin Doshi Department of Chemical and Biochemical Engineering, Missouri University of Science and Technology, Rolla, MO 65409, United States
[b] Gas Technology Institute, 1700 South Mount Prospect Road, Des Plaines, IL 60018, United States
[c] Center for Nanoscale Materials, Argonne National Laboratory, 9700 S. Cass Avenue, Argonne, IL 60439, United States

ARTICLE INFO

Keywords:
ZrO_2 overcoating
Atomic layer deposition (ALD)
Dry reforming of methane (DRM)
Metal-oxide interface
Oxygen vacancy

ABSTRACT

Zirconium oxide (ZrO_2) was deposited onto Ni/Al_2O_3 catalyst as overcoating by atomic layer deposition (ALD) for dry reforming of methane (DRM). High-temperature heating during H_2-reduction could transform the ALD-prepared ZrO_2 thin film to tetragonal phase and crack the encapsulating layer on Ni sites, which constructed a beneficial Ni-ZrO_x interface. Interfacial surface oxygen vacancies on ZrO_2 overcoating were induced by the partial reduction of ZrO_2 surface during high-temperature H_2 reduction, with the assistance of Ni. During DRM, the interfacial oxygen vacancies enhanced CO_2 activation by dissociating CO_2 and releasing active O, thereby limiting carbon formation. For DRM at 700 °C and 800 °C, Ni/Al_2O_3 with 5 cycles of ZrO_2 ALD overcoating enhanced both activity and stability significantly. For a 100-h DRM test at 600 °C, no deactivation was observed for the Ni/Al_2O_3 catalyst with 10 cycles of ZrO_2 ALD overcoating, as compared to 59% relative activity loss of Ni/Al_2O_3.

1. Introduction

Chemical utilization of carbon dioxide (CO_2) *via* dry reforming of methane (DRM) showed promising results in lowering the overall greenhouse gas carbon emission and in producing syngas (i.e., H_2 and CO) as valuable C1 building blocks [1,2]. Nickel, with low price and considerable initial activity, is widely studied as an attractive candidate for DRM [1,3]. However, deactivation of Ni catalysts due to coking and sintering remains a challenge for the implementation of Ni-based catalysts for DRM [3]. When the removal rate of carbon intermediate *via* CO_2 oxidation is lower than the formation rate of carbon intermediate from methane decomposition or Boudouard reactions, coke accumulates and leads to catalyst deactivation [4–6].

Efforts are made to construct the metal-oxide interface for the enhancement of catalytic performance. One strategy is to decrease the size of Ni nanoparticles (NPs) to increase the fraction of interfacial Ni sites and then utilize surrounding surface O species [7]; however, the sintering of Ni NPs during the high-temperature DRM reaction becomes problematic. Another strategy is to construct a metal-oxide interface and increase the interfacial oxygen species by introducing an oxide promoter or overcoating, such as CeO_2 [8], MgO [9], or ZrO_2 [10], onto the Ni-based catalysts. Especially, when Ni NPs are supported on or decorated by metal oxides, oxygen vacancies (V_o) surrounding the metal-oxide interface can participate in the dissociative activation of CO_2 to form active oxygen species, which is active for DRM and coke oxidation [4–6]. Considering the importance of interfacial oxygen species as CO_2 activation sites for DRM, the metal oxide overcoating decorating the Ni sites makes it imperative to create metal-oxide interface for the catalytic performance.

ZrO_2 was studied due to its thermal stability and basicity, and the deficient oxygen vacancies on ZrO_2 can serve as oxygen transfer sites for catalytic reactions [11]. Notably, the reduction treatment on ZrO_2 can partially remove the oxygen atoms and induce the formation of oxygen vacancies with the coordinatively unsaturated zirconium sites (Zr_{cus}) [12,13]. Zhang *et al.* investigated the pretreatment (using N_2, O_2, or H_2) on Ni/ZrO_2 for DRM and found that H_2-treatment promoted the formation of surface oxygen species (including oxygen vacancies) [14]. Studies also showed that H_2-active metal NPs on reducible oxides promoted the reduction of the neighboring oxygen *via* hydrogen spillover, thereby decreasing the formation energy of interfacial oxygen vacancy *via* the charge compensation [12,13]. Therefore, the oxygen species on the ZrO_2 overcoating should be studied to improve the performance in DRM catalyst development.

Different from the traditional wet chemistry coating (normally

* Corresponding author.
E-mail address: Liangxin@mst.edu (X. Liang).

https://doi.org/10.1016/j.cej.2022.135195
Received 6 October 2021; Received in revised form 1 February 2022; Accepted 7 February 2022
Available online 10 February 2022

20–30 nm thick) [15,16], atomic layer deposition (ALD), which is a layer-by-layer thin film coating technique, can introduce unique interfacial overcoating and tailor metal-oxide interface at atomic levels *via* self-limiting reactions for nano-engineered catalysts [17,18]. As for DRM, Al_2O_3 ALD has been reported to improve the catalyst stability [19,20]; however, due to the coverage of Ni sites by inert Al_2O_3 and the formation of $NiAl_2O_4$ [21,22], the enhanced stability was achieved at the cost of catalytic activity (see summary in Table S1 [19,20,23–26]). Therefore, depositing ZrO_2 overcoating with surface oxygen species is promising to construct an ideal metal-oxide interface and enhance CO_2 activation for enhanced catalytic performance. In this work, ALD was used to deposit various amounts of ZrO_2 overcoating onto Ni/Al_2O_3 catalyst. The metal-oxide interface constructed by ZrO_2 ALD overcoating enhanced CO_2 activation and improved the activity and stability of Ni/Al_2O_3 catalyst, as ascribed to the reduction-induced oxygen vacancies at the metal-oxide interface.

2. Experimental

2.1. Catalyst preparation

The Ni/Al_2O_3 catalyst was prepared by a traditional incipient wetness method. Commercial γ-Al_2O_3 NPs (Sigma Aldrich), with an average particle size of 50 nm and a BET surface area of 137 m^2/g, were used as support. The γ-Al_2O_3 NPs were soaked in an aqueous solution with nickel nitrate ($Ni(NO_3)_2{\cdot}6H_2O$, Sigma-Aldrich, 97%) for 1 h, and then were dried in an oven at 100 °C overnight. The dried particles were calcined at 500 °C in air in a tubular furnace for 3 h to remove the nitride component. In this work, the loading of Ni was ~4.7 wt% for Ni/Al_2O_3 catalyst.

Various cycles of ZrO_2 ALD were deposited on the pristine Ni/Al_2O_3 catalysts using a home-made fluidized bed ALD reactor [27], as shown in Figure S1. Tetrakis (dimethylamido) zirconium (IV) (TDMAZ, Sigma-Aldrich, 99.99%) and deionized water were used as precursors. Typically, Ni/Al_2O_3 sample was loaded into the ALD reactor and heated at 150 °C overnight to remove physically adsorbed moisture. The reaction temperature was 200 °C, and N_2 (Airgas, 99.9%) was used as a carrier gas for a TDMAZ bubbler or a flush gas to remove excess precursors and by-products from the reactor system. One ALD cycle consisted of TDMAZ precursor dose, N_2 purge, evacuation, deionized water dose, N_2 purge, and evacuation. 2, 5, and 10 cycles of ZrO_2 ALD were applied on the Ni/Al_2O_3 sample, labeled as $2ZrO_2$-Ni/Al_2O_3, $5ZrO_2$-Ni/Al_2O_3, and $10ZrO_2$-Ni/Al_2O_3, respectively.

For comparison, the incipient wetness method was also used to add ZrO_2 onto Ni/Al_2O_3 catalyst with the same ZrO_2 contents as $2ZrO_2$-Ni/Al_2O_3, $5ZrO_2$-Ni/Al_2O_3, and $10ZrO_2$-Ni/Al_2O_3, respectively. The Ni/Al_2O_3 catalyst was soaked in a zirconium (IV) oxynitrate ($ZrO(NO_3)_2{\cdot}xH_2O$, Alfa Aesar, 99.9%) solution for 1 h, dried at 100 °C, and then calcined at 500 °C in air for 3 h.

2.2. Dry reforming of methane reaction

The DRM reaction was carried out using a homemade gas phase reactor system, consisting of a vertical quartz tube (I.D. 10 mm), a tube furnace, and an on-line gas chromatograph (SRI 8610C). A K-type thermocouple (Omega Engineering) was applied to measure the temperature of the catalyst inside the reactor. Mass flow controllers (MKS Instruments) were used to control gas flow rates. For the DRM test, catalyst particles (~50 mg) were supported by quartz wool (~30 mg) in the reactor. The samples underwent a reduction process at 800 °C in a gas flow of 100 mL/min with H_2/Ar (mixed at 20/80 vol%, Airgas, UHP level) for 1 h. After reduction, the inlet gas was switched to a reactant gas of CH_4/CO_2 (mixed at 50/50 vol%, Airgas, UHP level) at a flow rate of 60 mL/min. The on-line gas chromatograph was equipped with a 6-foot Hayesep D column (for H_2, CO, and CH_4), a 6-foot molecular sieve 13X column (for CO_2 and H_2O), and a thermal conductivity detector (TCD) was used for gas component analysis. The conversions and H_2/CO molar ratios were calculated based on the following:

$$X_{CH4} = (1 - \frac{F_{CH4,out}}{F_{CH4,in}}) \times 100\% \quad (1)$$

$$X_{CO2} = (1 - \frac{F_{CO2,out}}{F_{CO2,in}}) \times 100\% \quad (2)$$

$$\frac{H_2}{CO} = \frac{F_{H2,out}}{F_{CO,out}} \quad (3)$$

2.3. Catalyst characterizations

Transmission electron microscopy (TEM, using an FEI Tecnai F20 TEM) was conducted to obtain the morphology of fresh and spent catalysts. X-ray photoelectron spectroscopy (XPS, using a Kratos Axis 165 X-ray photoelectron spectrometer) was conducted to obtain the chemical states of elements. X-ray diffraction (XRD, using Philips X-Pert Multipurpose Diffractometer) was conducted to obtain the crystalline information of the catalyst samples. Inductively coupled plasma-optical emission spectroscopy (ICP-OES) was conducted to analyze the element contents on the catalysts using 2000D Perkin Elmer (results in Table S2). The digestion of the samples was achieved with a 16-position pressure vessel Titan MPS microwave instrument. Raman spectra measurements were conducted on a Horiba Jobin-Yvon LabRam with a HeNe laser (λ = 633 nm).

Hydrogen temperature-programmed reduction (H_2-TPR) and H_2 pulse chemisorption were performed with a Micromeritics AutoChem II 2920 instrument. The TPR test started with a preheating treatment at 500 °C in Ar, then it was cooled to room temperature in Ar flow, and finally temperature ramping from room temperature to 1,000 °C at 10 °C/min with a gas flow of H_2/Ar (mixed at 10/90 vol%) was used. The H_2 pulse chemisorption consisted of a reduction in H_2/Ar (mixed at 10/90 vol%) flow at 700 °C for 1 h, a flush in Ar at 700 °C for 1 h, cooling to 50 °C in Ar, and pulse chemisorption of H_2 at 50 °C. The amount of H_2 uptake was calibrated by the TPR profile of Ag_2O standard. The surface area was estimated as follows:

$$S_{Ni} = \frac{N_H N_A z}{m_{cat}\sigma_{Ni}} \quad (4)$$

where S_{Ni} is the surface area, m^2/g, N_H is the amount of adsorbed H_2, mol, N_A is the Avogadro's constant, 6.02×10^{23}, z is 2 for dissociative chemisorption of H_2 on Ni, m_{cat} is the mass of catalyst for H_2 chemisorption, g, and σ_{Ni} is the number of Ni atoms per unit area, 1.54×10^{19} m^{-2}.

Temperature-programed surface reaction (TPSR), temperature-programed oxidation (TPO), and temperature-programed desorption (TPD) were performed in a quartz tube reactor with a QMS200 gas analyzer mass spectrometer (Stanford Research System). The gas species were identified according to the m/e value of MS signal; for example, Ar at 40, H_2 at 2, CH_4 at 16, CO at 28, CO_2 at 44, and O_2 at 32. Sequential CH_4-TPSR/CO_2-TPO/O_2-TPO for the reduced catalysts consisted of reduction in 20 mL/min H_2/Ar (mixed at 20/80 vol%) at 800 °C, cooling to 100 °C in Ar, CH_4-TPSR in 20 mL/min CH_4/Ar (mixed at 20/80 vol%) from 100 to 850 °C, cooling to 100 °C in Ar, CO_2-TPO in 20 mL/min CO_2/Ar (mixed at 20/80 vol%) from 100 to 850 °C, cooling to 100 °C in Ar, and O_2-TPO in 20 mL/min O_2/Ar (mixed at 20/80 vol%) from 100 to 850 °C. The CO_2-TPD consisted of pretreatment in Ar at 800 °C for fresh catalysts or reduction in H_2/Ar (mixed at 20/80 vol%) at 800 °C for reduced catalysts. Then, the catalysts were cooled to 80 °C in Ar, kept in 20 mL/min CO_2/Ar (mixed at 20/80 vol%) at 80 °C for 1 h, kept in Ar at 80 °C for 1 h, and then heated in Ar from 80 °C to 700 °C. The O_2-TPO of spent catalysts included pretreatment in Ar at 100 °C for 1 h and oxidation in 20 mL/min O_2/Ar (mixed at 20/80 vol%) from 100 °C to 800 °C.

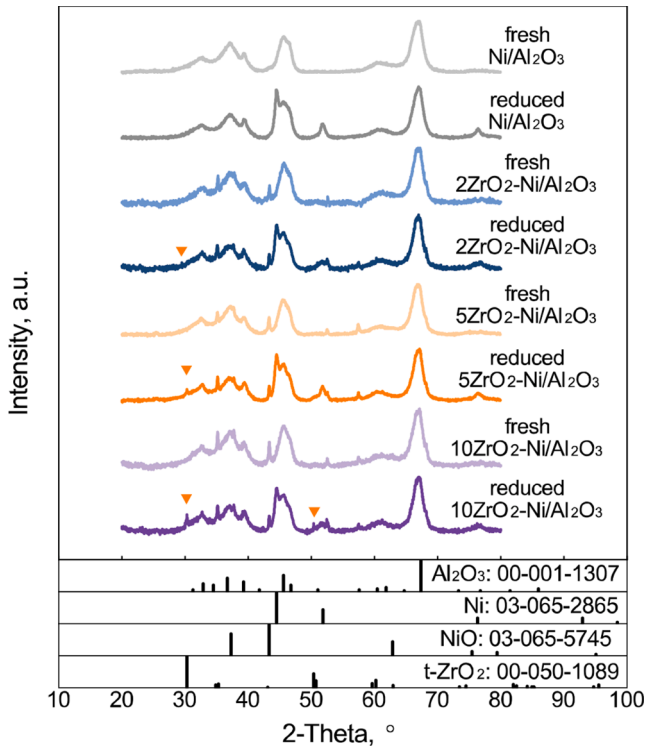

Fig. 1. XRD profiles of fresh Ni/Al_2O_3, reduced Ni/Al_2O_3, reduced Ni/Al_2O_3, fresh $2ZrO_2$-Ni/Al_2O_3, reduced $2ZrO_2$-Ni/Al_2O_3, fresh $5ZrO_2$-Ni/Al_2O_3, reduced $5ZrO_2$-Ni/Al_2O_3, fresh $10ZrO_2$-Ni/Al_2O_3, and reduced $10ZrO_2$-Ni/Al_2O_3.

2.4. Kinetic study

Kinetic measurement was conducted in the same reactor system as the catalytic performance test. The feed gas consisted of CH_4, CO_2, and Ar. Partial pressure of one reactant gas varied from 10 kPa to 45 kPa, and the other reactant gas was set at 30 kPa. The Ar was set to keep the total pressure at 101 kPa and a total flow rate of 101 mL/min. The temperature range was 500 °C to 575 °C, with all conversions < 20%. The external and internal mass transfer limitations were excluded, as verified by the Mear criterion [28] and Weisz-Prater criterion [29] (see Supporting Information for details). The reaction rate was expressed as the function of reactant partial pressure using the power-law model, as follows:

$$r_{CH4} = kP_{CH4}{}^{a}P_{CO2}{}^{b} \quad (5)$$

where k is the rate constant, and a and b are the orders of the reaction to be determined. The activation energy could be determined according to the following Arrhenius equation:

$$lnk = -\frac{E_a}{RT} + lnA \quad (6)$$

where E_a is the activation energy, T is absolute temperature, and A is the pre-exponential factor.

3. Results and discussion

3.1. Material characterizations

3.1.1. Structure and morphology characterizations

XRD was employed to investigate the crystalline structure of catalysts, including fresh Ni/Al_2O_3, reduced Ni/Al_2O_3, fresh $xZrO_2$-Ni/Al_2O_3, and reduced $xZrO_2$-Ni/Al_2O_3 (x = 2, 5, or 10, reduced catalysts underwent reduction process at 800 °C in 100 mL/min 20vol%/80 vol% H_2/Ar). As shown in Fig. 1, most of the peaks aroused from γ-Al_2O_3 with cubic structure, with peaks at 37.7°, 39.5°, 45.9°, 60.8°, and 66.9° for (311), (222), (400), (333), and (440) planes of γ-Al_2O_3, respectively. The peaks of NiO were not obvious, probably due to the formation of $NiAl_2O_4$ or because of overlapping by intense Al_2O_3 peaks. For the fresh Ni/Al_2O_3 and the fresh $xZrO_2$-Ni/Al_2O_3 samples, the peaks located at 37.2°, 43.4°, and 62.8° were identified as (111), (200), and (220) planes of NiO, respectively. After reduction, the peaks of metallic Ni appeared for the reduced Ni/Al_2O_3 and the reduced $5ZrO_2$-Ni/Al_2O_3 samples. As for ZrO_2, the XRD patterns of reduced $xZrO_2$-Ni/Al_2O_3 samples exhibited tetragonal ZrO_2 (t-ZrO_2). Due to the unique growth process of ZrO_2 ALD and ultrathin film structure, the formation of the amorphous and the tetragonal phases has been reported [30,31]. Thus, the peak located at 30.3° was assigned to the (011) plane of t-ZrO_2 for the reduced $2ZrO_2$-Ni/Al_2O_3 and reduced $5ZrO_2$-Ni/Al_2O_3 catalysts. Peaks located at 30.3° and 50.4° were assigned to the (011) and (112) of t-ZrO_2 for the reduced $10ZrO_2$-Ni/Al_2O_3 catalyst. Notably, these t-ZrO_2 peaks were more significant for the reduced $xZrO_2$-Ni/Al_2O_3 catalysts than the fresh $xZrO_2$-Ni/Al_2O_3 catalysts, thus indicating that more t-ZrO_2 formed due to the high-temperature process. The crystalline transformation towards more t-ZrO_2 led to structure change, which possibly caused the cracking of the encapsulating layer. Studies showed that the high-temperature treatment led to structure change and cracking of the ALD thin film [32,33]. In this case, the moderate structure change and the possible cracking of ZrO_2 ALD layer effectively enabled the exposure of the active nickel sites to the reactant gases.

The morphologies of the catalysts were obtained using TEM, as shown in Fig. 2, Figure S2, and Figure S3. For the reduced Ni/Al_2O_3 catalyst, the average size of Ni NPs was approximately 13.5 nm (Fig. 2a), whereas the size of Ni NPs for $5ZrO_2$-Ni/Al_2O_3 was approximately 12.6 nm (Fig. 2b). The presence of ZrO_2 overcoating prevented the sintering of Ni NPs during the high-temperature reduction process. Regarding ZrO_2 morphology, the results of elemental mapping (see Fig. 2c) showed that the ZrO_2 overcoating grew on both Ni NPs and Al_2O_3 substrate. Onn *et al.* applied ZrO_2 ALD on PdO/Al_2O_3 for methane oxidation and found that the ZrO_2 layer after high-temperature treatment exhibited small chunks and thin layer structure based on EDS mapping analysis [33]. In this study, the ZrO_2 (Fig. 2c) after high-temperature reduction was also less uniform than the pristine ALD-prepared ZrO_2 film on the fresh catalyst (Figures S2 and S3), which indicates that the structure of ZrO_2 film changed after high-temperature reduction.

3.1.2. Interaction of ZrO_2 overcoating, Ni sites, and Al_2O_3

The H_2-TPR was conducted to determine the interaction between NiO and Al_2O_3 for the Ni/Al_2O_3 and ZrO_2-overcoated Ni/Al_2O_3 catalysts, as shown in Fig. 3 with quantitative results in Table S3. For the Ni/Al_2O_3 catalyst, the metal-oxide interaction between Ni and Al_2O_3 depends on the extent of NiO diffusion into Al_2O_3 [8,34]. Notably, $NiAl_2O_4$, a spinel crystalline with strong stability, needs a high reduction temperature of approximately 800 °C, whereas NiO without interaction can be reduced at 400 °C [29]. The species with reduction temperatures at 500–700 °C is identified as NiO-Al_2O_3 (or called nonstoichiometric $NiAl_xO_y$) [29]. As shown in Fig. 3a, TPR profiles for Ni/Al_2O_3 were deconvoluted into three peaks at ~285 °C, ~617 °C, and ~793 °C. The peak at ~285 °C was assigned to a small amount of amorphous nano-sized NiO, which was reduced at a lower temperature than that of the bulk NiO. As for the peak at higher temperatures, the Ni(II) peak at ~617 °C was NiO-Al_2O_3, and the Ni(II) peak at ~793 °C was spinel $NiAl_2O_4$. For the ZrO_2-Ni/Al_2O_3 catalyst, the reduction peaks of Ni/Al_2O_3 shifted toward lower temperatures than those of Ni/Al_2O_3; the peak assigned to NiO-Al_2O_3 shifted from ~617 °C to ~590 °C, and the peak assigned to $NiAl_2O_4$ shifted to ~764 °C. Moreover, the fraction of NiO-Al_2O_3 increased, whereas the fraction of $NiAl_2O_4$ decreased. Consequently, the metal-oxide interaction between NiO and Al_2O_3 was weakened by ZrO_2 during reduction, and the reducibility of Ni/Al_2O_3 was enhanced, which was attributed to the formation of intimate Ni-ZrO_x interfaces. The enhanced reducibility of Ni/Al_2O_3 by ZrO_2 led to a

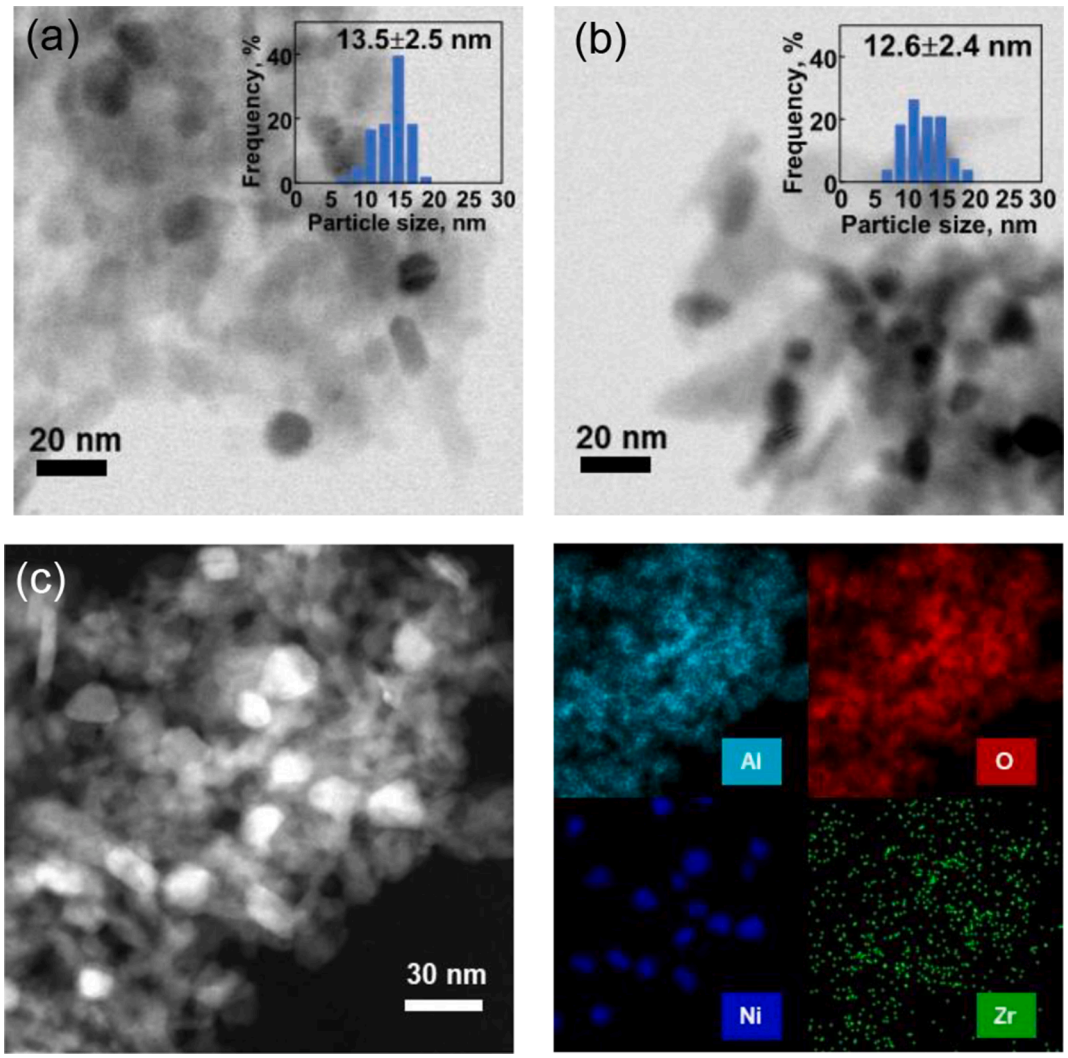

Fig. 2. TEM images of (a) reduced Ni/Al_2O_3 and (b) reduced $5ZrO_2$-Ni/Al_2O_3, (c) EDS elemental mapping of Al, O, Ni, and Zr for the reduced $5ZrO_2$-Ni/Al_2O_3 catalyst. The insets show the Ni particle size distributions.

higher fraction of metallic nickel during the redox atmosphere in DRM.

In addition, TPR was applied to probe the cracking of ZrO_2 ALD on Ni/Al_2O_3, as shown in Fig. 3b. In this work, all samples underwent heat pretreatment before TPR with pretreatment temperatures at 100 °C, 300 °C, 500 °C, and 700 °C (note: 500 °C in Fig. 3a). Notably, there was a small peak at 260 °C, which was assigned to free NiO for $5ZrO_2$-Ni/Al_2O_3 pretreated at 500 °C, and this peak shifted to a higher temperature for the $5ZrO_2$-Ni/Al_2O_3 catalyst that was pretreated at 100 °C or 300 °C. The peaks assigned to NiO-Al_2O_3 or $NiAl_2O_4$ remained at similar positions. The shifting of free NiO peaks confirmed that NiO was covered/confined by ZrO_2 until the cracking of the ZrO_2 ALD layer during the high-temperature pretreatment, which was similar to that reported in the literature [18]. The peaks for $5ZrO_2$-Ni/Al_2O_3 pretreated at 100 °C or 300 °C were notably asymmetric, which also indicated the confinement effect of ZrO_2. The pretreatment at 700 °C in Ar led to the shifting of all peaks towards high temperatures, indicating that a calcination process at excessive temperatures strengthened the interaction between NiO and Al_2O_3. In this study, high temperature (800 °C) during the reduction for DRM already exceeded the cracking temperature of ZrO_2 thin film and thus helped the exposure of nickel sites. Compared with encapsulating structure, the cracked ZrO_2 overcoating after high-temperature reduction exposed Ni active sites for CH_4 dissociation and provided sufficient Ni-ZrO_x interface for better catalytic performance.

3.1.3. *Effects of H_2 treatment*

High resolution XPS was conducted to determine the chemical states of fresh Ni/Al_2O_3, fresh $5ZrO_2$-Ni/Al_2O_3, reduced Ni/Al_2O_3, and reduced $5ZrO_2$-Ni/Al_2O_3 (see Fig. 4, Table S4, and Figure S4). All spectra were calibrated by using the adventitious carbon of C1s at 284.5 eV (Figure S4). For Ni2p in the Ni/Al_2O_3 catalyst, the Ni2p3/2 peaks were generally deconvoluted into metallic Ni, NiO, spinel $NiAl_2O_4$, and satellite peaks for Ni(0) and Ni(II) [8,35]. Notably, Ni/Al_2O_3 and $5ZrO_2$-Ni/Al_2O_3 had identical profiles, exhibiting peaks of NiO at ~855.3 eV, $NiAl_2O_4$ at ~856.9 eV, and satellite peak of Ni^{2+} at ~861.7 eV. The identical profiles indicated that the ZrO_2 ALD overcoating did not affect the interaction between Ni and Al_2O_3, probably due to the low deposition temperature of ZrO_2 ALD. After the samples underwent the reduction process, the peaks for metallic Ni at ~852.1 eV and satellite peak of Ni(0) at ~858.5 eV appeared for the reduced Ni/Al_2O_3 and reduced $5ZrO_2$-Ni/Al_2O_3 samples. The NiO in the reduced samples was resulted from the oxidation by air during sample transportation. The $NiAl_2O_4$, with low reducibility and inert DRM activity, was less in the reduced $5ZrO_2$-Ni/Al_2O_3 sample due to the ZrO_2 overcoating, which is consistent with the TPR results.

As for O1s in Fig. 4b, the oxygen peaks were deconvoluted into lattice O at 530.4 eV (mainly metal oxide) and surface O at 531.4 eV (including low-coordination oxygen, hydroxyl oxygen, and adsorbed H_2O) [14,35]. The fresh Ni/Al_2O_3 and reduced Ni/Al_2O_3 samples had

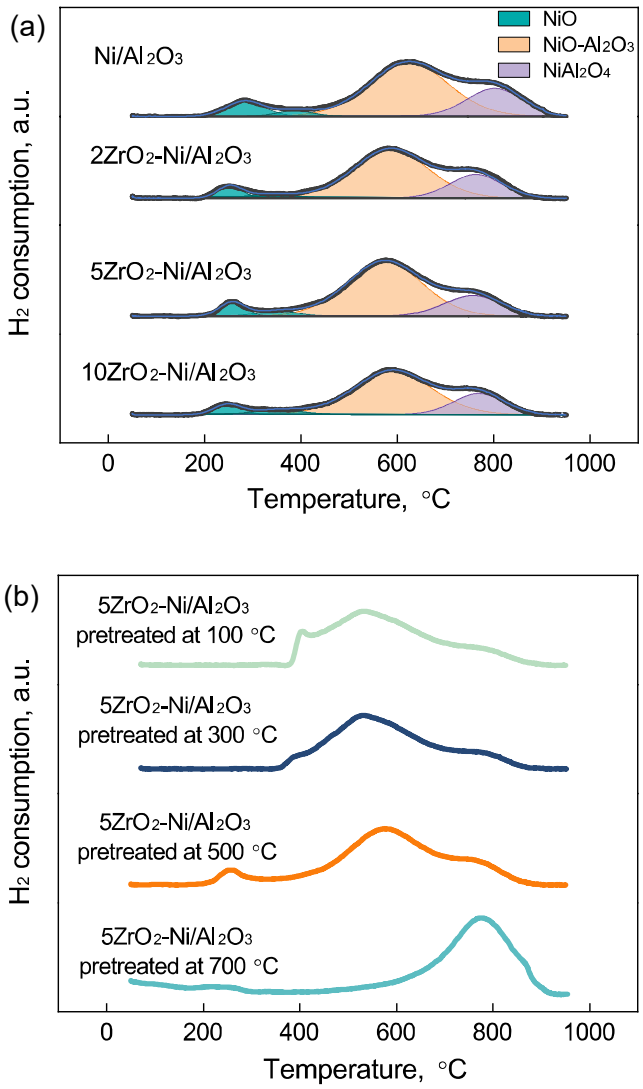

Fig. 3. (a) H_2-TPR profiles of Ni/Al_2O_3, $2ZrO_2$-Ni/Al_2O_3, $5ZrO_2$-Ni/Al_2O_3, and $10ZrO_2$-Ni/Al_2O_3 with pretreatment at 500 °C, and (b) H_2-TPR profiles of $5ZrO_2$-Ni/Al_2O_3 with pretreatment at 100, 300, 500, and 700 °C.

identical profiles, indicating that the chemical states of O for Ni/Al_2O_3 remained the same after the reduction in H_2 and recovery in air. With the introduction of ZrO_2 overcoating onto Ni/Al_2O_3, there was an increased amount of surface oxygen for the fresh $5ZrO_2$-Ni/Al_2O_3 catalyst, from 21% for the fresh Ni/Al_2O_3 catalyst to 30% for the fresh $5ZrO_2$-Ni/Al_2O_3 catalyst, which was ascribed to the larger amount of hydroxyl groups on ZrO_2 than those on Al_2O_3. The surface oxygen for the reduced $5ZrO_2$-Ni/Al_2O_3 sample was further increased to 37%, as compared to that of the fresh $5ZrO_2$-Ni/Al_2O_3 sample, whereas the surface oxygen was only 21% for the fresh Ni/Al_2O_3 sample and 20% for the reduced Ni/Al_2O_3 sample. There was an additional surface oxygen species generated on ZrO_2 overcoating during the reduction process.

Different from bulk ZrO_2 that was primarily composed of stoichiometric ZrO_2 [12,36], the Zr 3d profiles of ZrO_2 ALD overcoating exhibited both stoichiometric ZrO_2 (182.4 eV for Zr 3d3/2 and 184.7 eV for Zr 3d1/2) and nonstoichiometric ZrO_x (181.4 eV for Zr 3d3/2 and 183.8 eV for Zr 3d1/2). The existence of nonstoichiometric ZrO_x could be attributed to the unique ALD growth process or subnano-size structure, and similar phenomena were reported for ZrO_2 thin film [37–39]. A lower amount of stoichiometric ZrO_2 (19%) was found for the reduced $5ZrO_2$-Ni/Al_2O_3 sample, as compared to 26% for the fresh $5ZrO_2$-Ni/Al_2O_3 sample, which indicated the partial reduction of ZrO_2 overcoating occurred during the reduction of the catalyst. For the partial reduction of ZrO_2, the removal of surface O by H_2 led to the formation of the oxygen vacancy site (V_o) [40,41]. The surrounding metal sites at the Ni-ZrO_x interface induced the partial reduction of ZrO_x [13,40,41]. Pacchioni *et al.* investigated the reduction behavior of ZrO_2 films on Pt_3Zr or Pt, and they determined that the metal sites could lower the formation energy of oxygen vacancies on the ZrO_2 surface in a H_2 atmosphere [41]. Hydrogen-active metals have been proven to enhance the reducibility of interfacial ZrO_2 and increase the concentration of surface oxygen vacancies [13]. The XPS study was also conducted to examine the effects of

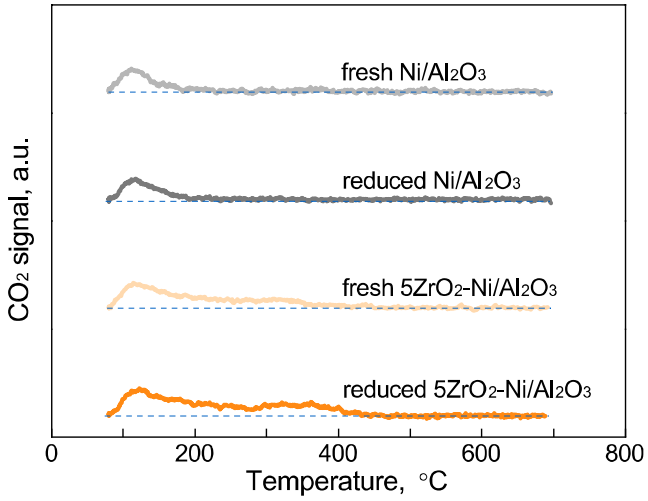

Fig. 5. CO_2-TPD of fresh Ni/Al_2O_3, reduced Ni/Al_2O_3, fresh $5ZrO_2$-Ni/Al_2O_3, and reduced $5ZrO_2$-Ni/Al_2O_3.

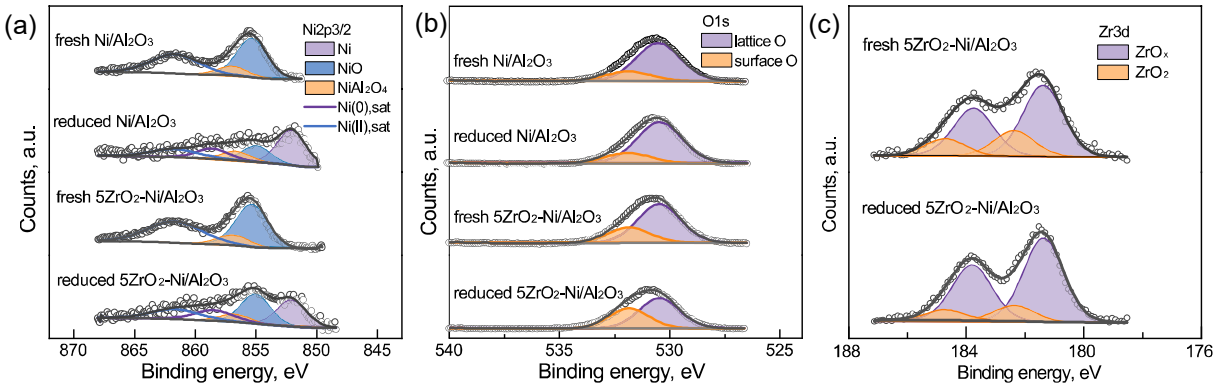

Fig. 4. XPS spectra of (a) Ni 2p3/2, (b) O 1 s, and (c) Zr 3d core levels of fresh Ni/Al_2O_3, reduced Ni/Al_2O_3, fresh $5ZrO_2$-Ni/Al_2O_3, and reduced $5ZrO_2$-Ni/Al_2O_3.

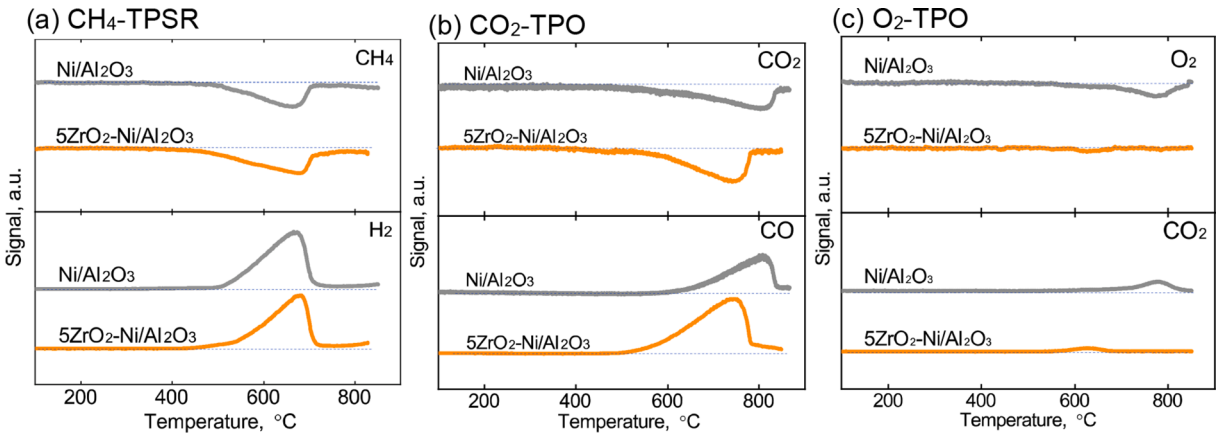

Fig. 6. Sequential CH_4-TPSR/CO_2-TPO/O_2-TPO for reduced Ni/Al_2O_3 and reduced $5ZrO_2$-Ni/Al_2O_3 catalysts: (a) CH_4-TPSR, (b) CO_2-TPO, and (c) O_2-TPO. All catalysts underwent a reduction process at 800 ℃ before the tests.

Ni sites using the fresh and reduced $5ZrO_2$-Al_2O_3 samples without the presence of Ni. As shown in Figure S5, without Ni, the fresh and the reduced $5ZrO_2$-Al_2O_3 samples exhibited similar surface oxygen levels in O 1 s and nonstoichiometric ZrO_x in Zr 3d. The difference between $5ZrO_2$-Al_2O_3 and $5ZrO_2$-Ni/Al_2O_3 indicated that the presence of Ni assisted the partial reduction of the surface O at interfacial ZrO_2. When the samples were cooled to room temperature, the low-coordinated oxygen or hydroxyl was recovered by air, which accounted for the increased surface oxygen for the ZrO_2-overcoated Ni/Al_2O_3 samples after reduction. Consequently, the partial reduction of ZrO_2 overcoating and the formation of surface oxygen sites were boosted by the ALD-prepared ZrO_2 overcoating and the presence of Ni.

CO_2-TPD was conducted to determine the adsorption and activation behavior of CO_2, as shown in Fig. 5. For Ni/Al_2O_3, the peak at T < 180 °C (in Fig. 5) was identified as weak basic sites for physisorption and surface –OH groups (Brønsted basic sites) [35,42]. After ZrO_2 was deposited onto Ni/Al_2O_3, more peaks appeared for ZrO_2-Ni/Al_2O_3. The peak at 180–300 °C was identified as medium basic sites for Lewis acid-base pair Zr^{4+}–O^{2-}, and the peak over 300 °C was identified as strong basic sites for low-coordination oxygen sites (e.g., oxygen vacancy) [42]. Studies demonstrated that oxygen vacancies can trap one O of CO_2 molecule as monodentate carbonate, lengthen the C = O bonds, and further dissociate the adsorbed CO_2 into CO and adsorbed O* species at DRM conditions [2,42,43]. As ZrO_2 ALD was deposited onto Ni/Al_2O_3, the basic nature of ZrO_2 increased the quantity and strength of basic sites for Ni/Al_2O_3. A larger number of basic sites appeared for the reduced $5ZrO_2$-Ni/Al_2O_3 sample, especially the strong basic sites, as compared to those of the fresh $5ZrO_2$-Ni/Al_2O_3 sample. The increased strong basic sites after reduction confirmed that the additional interfacial oxygen vacancies were induced *via* the partial reduction of surface ZrO_2, and they thereby enhanced the CO_2 activation.

3.1.4. *Role of ZrO_2 overcoating in reactant activation*

To get further insight into the effects of ZrO_2, temperature-programed surface reaction (CH_4-TPSR) was conducted to test the activity of catalysts for CH_4, and the following temperature-programmed oxidation (CO_2-TPO and O_2-TPO) was conducted to demonstrate the capacity of catalysts in CO_2 activation and carbon removal, as shown in Fig. 6. In DRM, the adsorption and activation of CH_4 will take place on metallic Ni sites as the initial step to generate adsorbed H and CH_x-Ni, which reacts with CO_2 [44]. For CH_4-TPSR (Fig. 6a), both Ni/Al_2O_3 and $5ZrO_2$-Ni/Al_2O_3 exhibited similar profiles for CH_4 consumption and H_2 generation peaks. The CH_4 consumption peak confirmed the cracking of ZrO_2 layer after high-temperature reduction. The initial temperatures for the CH_4-consumption and H_2-generation peak started at a lower temperature (430 °C) for $5ZrO_2$-Ni/Al_2O_3, as compared to 470 °C for Ni/Al_2O_3, whereas the peak positions were located at approximately 670 °C for both catalysts. It was postulated that part of Ni showed better activity in dissociating CH_4 due to the ZrO_2 overcoating, because the average Ni size of ZrO_2-overcoated Ni/Al_2O_3 was smaller than that of the uncoated

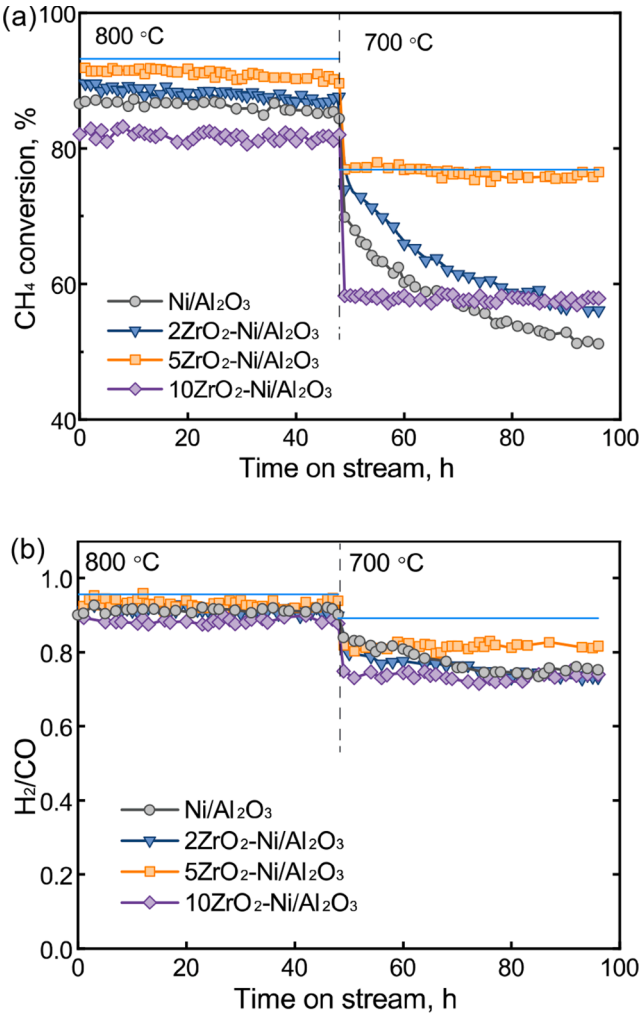

Fig. 7. (a) CH_4 conversion and (b) H_2/CO ratio of DRM using Ni/Al_2O_3, $2ZrO_2$-Ni/Al_2O_3, $5ZrO_2$-Ni/Al_2O_3, and $10ZrO_2$-Ni/Al_2O_3 at 700 ℃ and 800 ℃. Reaction conditions: 50 mg catalyst, 30 mL/min CH_4, and 30 mL/min CO_2. The blue solid lines show the equilibrium values.

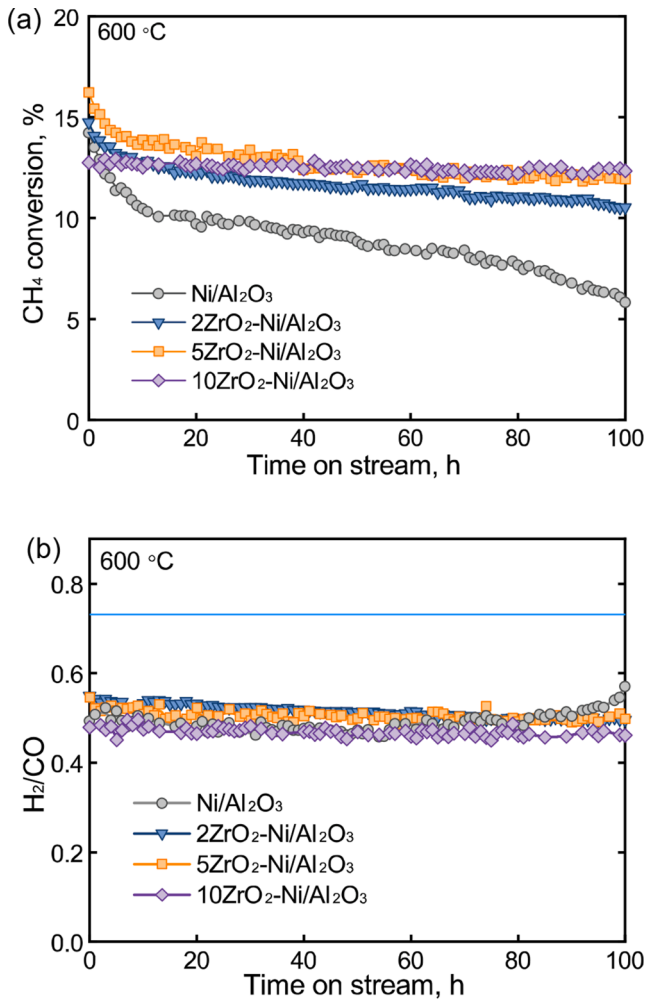

Fig. 8. (a) Methane conversion and (b) H_2/CO ratio of DRM using Ni/Al_2O_3, $2ZrO_2$-Ni/Al_2O_3, $5ZrO_2$-Ni/Al_2O_3, and $10ZrO_2$-Ni/Al_2O_3 at 600 °C. Reaction conditions: 50 mg catalyst, 30 mL/min CH_4, and 30 mL/min CO_2. The blue solid lines show the equilibrium value. The equilibrium CH_4 conversion is 40.7% at the reaction conditions.

Ni/Al_2O_3 or part of Ni sites interacted with ZrO_2 overcoating and was influenced by ZrO_x [45].

For the oxidation of CH_x-Ni by CO_2, although this process can occur on nickel surface (often reported for solely Ni or Ni/SiO_2), a much more efficient pathway of CO_2 activation can take place on surface O at the metal-oxide interface and the active O from CO_2 dissociation further transfers towards Ni to oxidize the CH_x on Ni sites [6,46]. For CO_2-TPO, the $5ZrO_2$-Ni/Al_2O_3 catalyst exhibited a larger CO_2-consumption peak and a larger CO-generation peak that were both found at 750 °C, as compared to the peaks at 810 °C for Ni/Al_2O_3. The lower temperature of CO_2-consumption and CO-generation peak on $5ZrO_2$-Ni/Al_2O_3 indicated that the activation of CO_2 occurred more efficiently due to ZrO_2 overcoating, which was closely related to the increased surface oxygen sites. These sites participated in the CO_2 activation and greatly improved the oxidation of CH_x-Ni species. The left carbon deposition after CO_2-TPO was further examined by O_2-TPO. Most of the carbon was removed by CO_2 oxidation for $5ZrO_2$-Ni/Al_2O_3, whereas there was a lot of graphitic carbon (T > 700 °C in Fig. 6c) for Ni/Al_2O_3. The carbon could accumulate and possibly lead to catalyst deactivation. The combination of CO_2-TPO and O_2-TPO after CH_4-TPSR indicated that the ZrO_2 ALD overcoating could greatly improve CO_2 activation for DRM reaction.

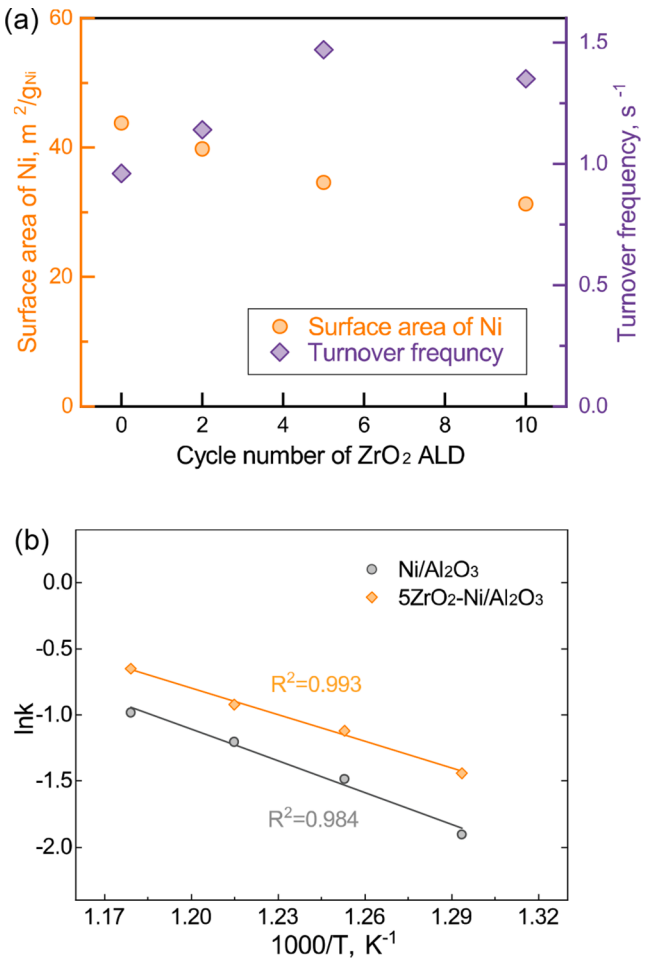

Fig. 9. (a) Effects of the number of ZrO_2 ALD cycles on Ni surface area based on H_2-chemisorption and turnover frequency of DRM at 600 °C. (b) Arrhenius plots for CH_4 activation energy during DRM using Ni/Al_2O_3 and $5ZrO_2$-Ni/Al_2O_3 as catalysts.

3.2. Catalytic performance

3.2.1. High-temperature DRM

To verify the role of oxygen vacancies formed at the metal-oxide interface by depositing ultra-thin ZrO_2 overcoating, the catalytic performance of pristine Ni/Al_2O_3 and ZrO_2 coated Ni/Al_2O_3 catalysts were tested and compared, as shown in Fig. 7 and Figure S6. The deposition of ZrO_2 exhibited a significant promoting effect for the Ni/Al_2O_3 catalyst. The $5ZrO_2$-Ni/Al_2O_3 sample showed the best performances in terms of stability and activity; the methane conversion reached 91.3% at 800 °C and 77.2% at 700 °C, as compared to 86.2% at 800 °C and 68.0% at 700 °C for the pristine Ni/Al_2O_3 catalyst. For $10ZrO_2$-Ni/Al_2O_3, the initial catalytic activity decreased to 81.5% at 800 °C and 57.2% at 700 °C, probably because too much ZrO_2 overcoating covered active sites of Ni/Al_2O_3, and the reactive sites were not fully exposed to the reactants. As for the stability, the 5 or 10 cycles of ZrO_2-overcoated Ni/Al_2O_3 catalysts exhibited excellent stability without any deactivation at both 800 °C and 700 °C, whereas the activity of Ni/Al_2O_3 catalyst decreased significantly from 68.0% to 52.6% at 700 °C.

The ZrO_2 ALD prepared samples were also compared to samples prepared by the traditional IW method. The ZrO_2 content of the IW-ZrO_2/Ni/Al_2O_3 sample was similar to those prepared by ALD. The sample was tested for DRM at 700 °C (see Figure S7). The highest initial CH_4 conversion of the IW-ZrO_2/Ni/Al_2O_3 catalyst with 1.4 wt% ZrO_2 (same as $10ZrO_2$-Ni/Al_2O_3) was 72.1%, which was lower than 77.2% for the $5ZrO_2$-Ni/Al_2O_3 catalyst. Besides, the IW-prepared IW-ZrO_2/Ni/

Al_2O_3 catalyst was less stable than the ALD-prepared ZrO_2-Ni/Al_2O_3 catalyst. There was a 9.7% relative activity loss for IW-ZrO_2/Ni/Al_2O_3 (1.4 wt% ZrO_2) and no deactivation loss for 5ZrO_2-Ni/Al_2O_3 and 10ZrO_2-Ni/Al_2O_3. The better performance of the ALD-prepared ZrO_2-Ni/Al_2O_3 catalysts than that of the IW-prepared catalysts was ascribed to the Ni-ZrO_x interface and oxygen species.

3.2.2. Low-temperature DRM

It is desirable to develop a highly stable catalyst at low operating temperatures. However, low temperature thermodynamically favored the formation reactions of coke (i.e., CH_4 decomposition and CO disproportionation) [47]. As shown in Fig. 8 and Figure S8, low-temperature DRM was tested, and the order of the initial reaction rate was determined as follows: 5ZrO_2-Ni/Al_2O_3 > 2ZrO_2-Ni/Al_2O_3 ≈ Ni/Al_2O_3 > 10ZrO_2-Ni/Al_2O_3. Rapid deactivation during the 100-h test from 14.2% to 5.8% (with 59% relative loss) was observed for the Ni/Al_2O_3 catalyst; in contrast, the deactivation rate of the 5ZrO_2-Ni/Al_2O_3 catalyst was slower (from 16.1% to 11.9%, with 26% relative loss), whereas the conversion of 2ZrO_2-Ni/Al_2O_3 catalyst decreased from 14.8% to 10.5% (with 30% relative loss). The H_2/CO ratio of DRM catalyzed by Ni/Al_2O_3 showed an increasing trend in the last 20 h of the reaction test, indicating the occurrence of the CH_4 catalytic decomposition without the following CO_2 oxidation. For the 10ZrO_2-Ni/Al_2O_3 catalyst, there was no deactivation during the DRM test for low-temperature DRM reaction at 600 °C. For both high-temperature and low-temperature DRM tests, the highest initial activity was achieved by 5ZrO_2-Ni/Al_2O_3, and the best stability was achieved by 10ZrO_2-Ni/Al_2O_3. The conclusion about the catalytic performance was drawn that a moderate amount of ZrO_2 overcoating was beneficial to a higher activity and the more amount of ZrO_2 overcoating achieved a better stability.

To clarify the confinement effects of ZrO_2 overcoating and the enhanced interfacial oxygen sites, the surface areas of active Ni for the reduced samples were determined by H_2 pulse chemisorption, as shown in Fig. 9a. Notably, the surface area gradually decreased when more cycles of ZrO_2 ALD were applied, indicating that part of Ni sites was covered by the ZrO_2 overcoating. The turnover frequency (TOF) values at 600 °C were driven to demonstrate the intrinsic rates for the DRM reactions ordered as follows: 5ZrO_2-Ni/Al_2O_3 > 10ZrO_2-Ni/Al_2O_3 > 2ZrO_2-Ni/Al_2O_3 > Ni/Al_2O_3. Higher TOF values of the ZrO_2-overcoated catalysts indicated that the ZrO_2 overcoating exhibited reaction-promoting effects and led to higher reaction rates. In this work, the sample with 5 cycles of ZrO_2 ALD film exhibited the highest turnover frequencies due to the moderate interfacial Ni-ZrO_x sites, though some of the Ni active sites were covered by the ZrO_2 overcoating. As more cycles of ZrO_2 ALD were applied, the intrinsic activity kept the same and the coverage of Ni sites could be detrimental to the overall methane conversion.

3.2.3. Activation energy measurement for DRM

The kinetic study was conducted for the Ni/Al_2O_3 and 5ZrO_2-Ni/Al_2O_3 catalysts to get deeper insight, as shown in Fig. 9b, Figure S9, and Table S5. By fixing the pressure of one reactant gas at 30 kPa and varying the pressure of the other reactant gas from 10 kPa to 45 kPa (balanced with Ar for a total pressure of 101 kPa), the relationships between reaction rates (in the express of CH_4) and reactant gas partial pressures was obtained. When comparing the reaction order, CH_4 with a higher reaction order had a greater impact on the reaction rate, which is consistent with the fact that CH_4 dissociation was the initial and dominant step [14,44]. The reaction order of CO_2 for 5ZrO_2-Ni/Al_2O_3 was lower than that of Ni/Al_2O_3, indicating that the less dependence of CO_2 partial pressure was ascribed to the active oxygen sites for the ZrO_2-overcoated Ni/Al_2O_3 catalysts. From the Arrhenius equation, the apparent activation energy of the reaction with the Ni/Al_2O_3 catalyst was approximately 71.1 kJ/mol, which is similar to values found in the literature [48–50]. In contrast, the apparent activation energy for 5ZrO_2-Ni/Al_2O_3 was lower (62.3 kJ/mol), confirming the promoting

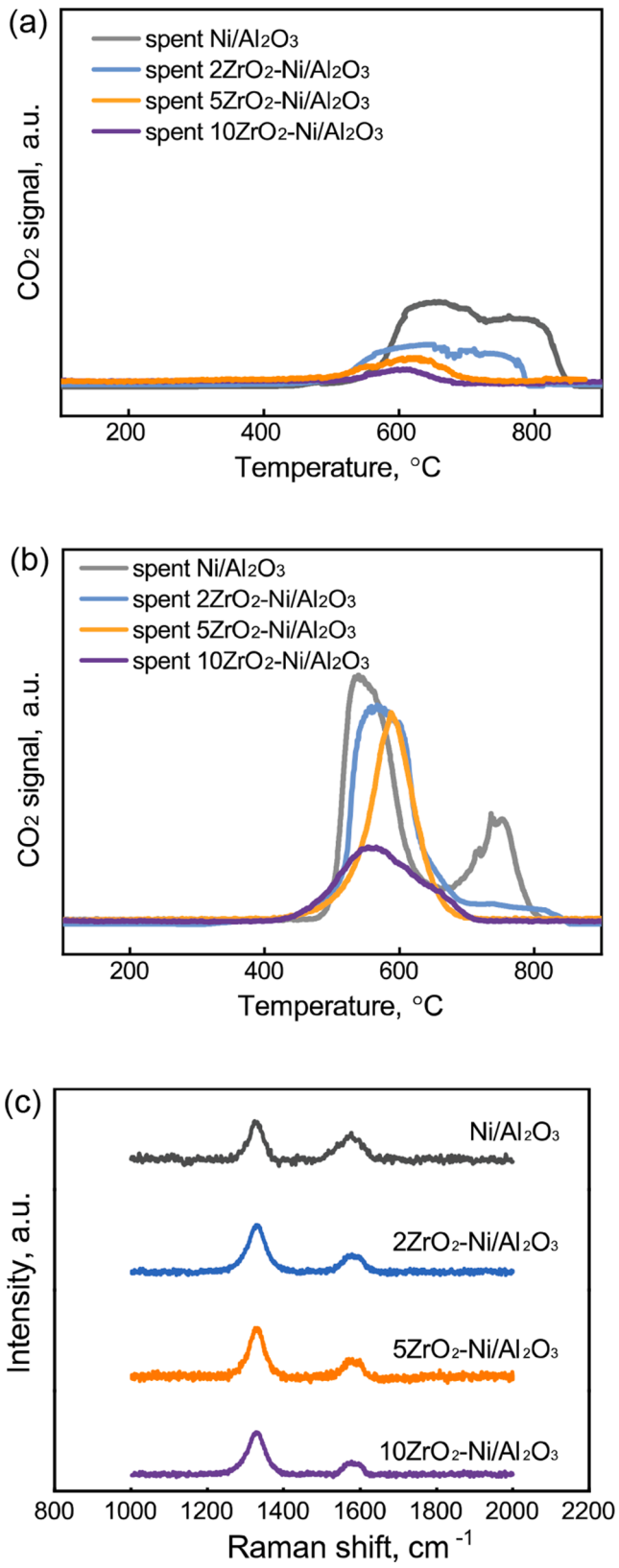

Fig. 10. TPO profiles of spent Ni/Al_2O_3, spent 2ZrO_2-Ni/Al_2O_3, spent 5ZrO_2-Ni/Al_2O_3, and spent 10ZrO_2-Ni/Al_2O_3: (a) after DRM at 800 °C for 48 h and 700 °C for 48 h sequentially, and (b) after DRM at 600 °C for 100 h. (c) Raman spectra for spent Ni/Al_2O_3, spent 2ZrO_2-Ni/Al_2O_3, spent 5ZrO_2-Ni/Al_2O_3, and spent 10ZrO_2-Ni/Al_2O_3 after DRM at 600 °C for 100 h.

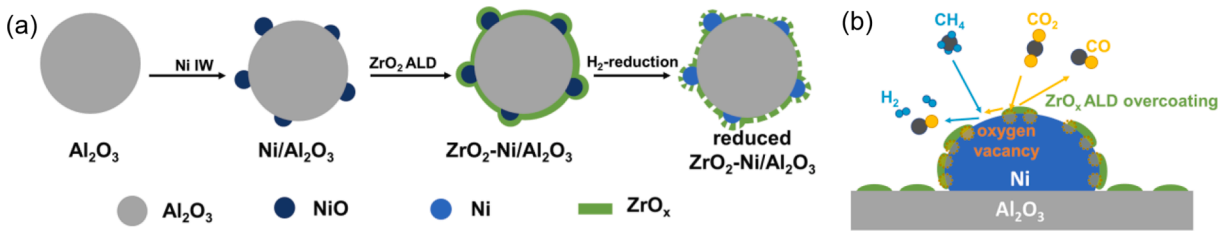

Fig. 11. Schematic representation of (a) catalyst preparation and catalyst reduction, (b) effects of ZrO_2 overcoating during the DRM reaction.

effect of the ZrO_2 overcoating.

3.3. Deactivation study

3.3.1. Sintering of Ni nanoparticles

The change of Ni NPs after DRM was checked by TEM. As shown in Figure S10, the spent Ni/Al_2O_3 catalyst had an average Ni size of 16.6 nm after DRM at 800 °C for 48 h followed by DRM at 700 °C for 48 h, whereas the $5ZrO_2$-Ni/Al_2O_3 catalyst had a smaller average Ni size of 14.9 nm after the same reaction time and conditions, which indicates that the ZrO_2 overcoating could prevent Ni sintering.

3.3.2. Coking formation

O_2-TPO was applied to study carbon deposition of the spent catalysts after DRM, as shown in Fig. 10 and carbon amount results in Table S6. Carbon with a TPO peak at 500–600 °C was identified as amorphous carbon, whereas the carbon requiring a higher oxidizing temperature was identified as graphitic carbon [15,46]. For the spent catalysts after reactions at 800 °C for 48 h and at 700 °C for 48 h sequentially, only small peaks appeared at approximately 610 °C for the $5ZrO_2$-Ni/Al_2O_3 catalyst or at approximately 625 °C for the spent $10ZrO_2$-Ni/Al_2O_3 catalyst (Fig. 10a). However, broad peaks were found for the spent Ni/Al_2O_3 and the spent ZrO_2-Ni/Al_2O_3 catalysts; the CO_2 signal peak (550 °C to 830 °C) for the spent Ni/Al_2O_3 catalyst indicated the existence of both amorphous and graphitic carbon. Therefore, the ZrO_2 ALD overcoating suppressed the formation of graphitic carbon. 5 cycles of ZrO_2 ALD film decreased 76% relative coke and 10 cycles of ZrO_2 decreased 90% relative coke of Ni/Al_2O_3 after DRM at 800 °C for 48 h and at 700 °C for 48 h sequentially. Similar results were obtained from the TPO result (Fig. 10b) of the spent catalysts after the 100-h DRM reaction at 600 °C. Due to the lower oxidation capacity for CO_2 at lower temperatures, the carbon deposition at 600 °C was more severe than that after the sequential DRM reactions at 800 °C and 700 °C. The severe coke after 100-h DRM test at 600 °C was found for Ni/Al_2O_3, reaching ~39.9 wt% of Ni/Al_2O_3; in contrast, the coke was only 11.8 wt% of the $10ZrO_2$-Ni/Al_2O_3 catalyst, indicating that the ZrO_2 layer decreased ~71% carbon deposition of Ni/Al_2O_3 at 600 °C. Only the spent Ni/Al_2O_3 and $2ZrO_2$-Ni/Al_2O_3 catalysts showed peaks above 700 °C, which indicates ZrO_2 overcoating effectively suppressed the formation of graphitic carbon.

To figure out the carbon nature after DRM, Raman spectra were conducted on the spent catalysts after 100-h DRM test at 600 °C (see Fig. 10c). All the catalysts exhibited 2 major peaks at ~1,340 cm^{-1} (D band) and ~1,580 cm^{-1} for (G band). The D band is the disorder-induced band from the structural imperfections in defective carbon, and the G band is the graphitic carbon with the in-plane C–C stretching vibrations of pairs of sp^2 carbon [51]. The intensity ratio I_D/I_G was calculated for the spent catalysts to represent the relative content for graphitic carbon. The lowest I_D/I_G ratio was achieved by the Ni/Al_2O_3 catalyst at ~1.6, indicating that Ni/Al_2O_3 had the most graphitic carbon among the tested catalysts. The I_D/I_G ratio reached ~2.4 for $2ZrO_2$-Ni/Al_2O_3, ~2.5 for $5ZrO_2$-Ni/Al_2O_3, and ~2.7 for $10ZrO_2$-Ni/Al_2O_3, indicating less graphitic carbon with more cycles of ZrO_2 ALD overcoating.

From TEM images for spent catalysts, there seem to be filamentous structure carbon for the spent Ni/Al_2O_3 catalyst (Figure S10b), whereas no such structure carbon was observed for the $5ZrO_2$-Ni/Al_2O_3 catalyst (Figure S10d). The filamentous carbon was generally assigned to the graphitic carbon and was generated due to the methane catalytic decomposition on Ni sites [46,52]. The TPO, Raman spectra, and TEM draw the consistent conclusion that the ZrO_2 overcoating suppressed the carbon formation, especially the graphitic carbon during the DRM reaction.

Based on the catalytic performance and carbon analysis from TPO and Raman, the deactivation was more closely related to the graphitic carbon than the amorphous carbon. For carbon species formed during DRM, the amorphous carbon was generally considered the product of the CH_4 thermal cracking on the whole catalyst, whereas the graphitic carbon with a well-ordered structure was generated from the catalytic dissociation of CH_4 on Ni sites [34,46,52]. The different growth sites of amorphous carbon and graphitic carbon could explain that the ZrO_2 overcoating improved suppression effects on the formation of graphitic carbon because the increased interfacial oxygen species on ZrO_2 overcoating around the Ni sites assisted the oxidation of carbon intermediate and prevented the growth of graphitic carbon. Therefore, the ZrO_2 overcoating on the Ni sites effectively suppressed the formation of graphitic carbon and enhanced the catalytic stability during DRM.

3.4. Mechanism of ZrO_2 overcoating

From the results of characterizations, including XRD, H_2-TPR, H_2-chemisorption, and CH_4-TPSR, the structure of the ZrO_2 layer significantly changed and the Ni sites became accessible to the reactant gases after high-temperature reduction. Based on these behaviors, it was postulated that the ZrO_2 layer was cracked during the high-temperature reduction process, although it was not directly observed. The cracked ZrO_2 overcoating still influenced the Ni sites (from XPS, H_2-TPR, CH_4-TPSR, and kinetics). Therefore, a hypothetical model was proposed that the cracked ZrO_2 overcoating remained on the Ni sites and further interacted with Ni (see reduced ZrO_2-Ni/Al_2O_3 in Fig. 11a). As schematically shown in Fig. 11a, high-temperature reduction before DRM not only reduced NiO to Ni, but also cracked the encapsulating ZrO_2 layer, which exposed Ni active sites and generated Ni-ZrO_x interface. The surface oxygen of ZrO_2 overcoating could be removed during H_2 reduction, possibly forming interfacial oxygen vacancies. During the DRM reaction (Fig. 11b), the oxygen vacancies at the Ni-ZrO_x interface participated in CO_2 dissociation as CO_2 activation sites and generated active adsorbed O* species. The active O* species further transferred to Ni sites and oxidized the carbon intermediates. The enhanced CO_2 activation by ZrO_2 ALD effectively prevented the formation of graphitic carbon. Therefore, ZrO_2 overcoating enhanced the activity and stability of Ni/Al_2O_3 for DRM.

4. Conclusion

In this work, ultrathin ZrO_2 overcoating was deposited by ALD onto IW-prepared Ni/Al_2O_3 catalysts for DRM. The high-temperature reduction process before the DRM reaction drove the ZrO_2 crystalline towards more tetragonal ZrO_2, which possibly cracked the ZrO_2 layer and

exposed Ni active sites. The reducibility of Ni(II) was improved by the metal-oxide interaction between Ni NPs and ZrO_2, which helped keep Ni in the metallic state. In addition, the high-temperature H_2 treatment partially removed the interfacial oxygen of ZrO_2 overcoating and induced the formation of oxygen vacancies on ZrO_2. The increased oxygen sites at the Ni-ZrO_x interface kinetically accelerated the CO_2 activation for DRM, thus improving the activity and stability for DRM, even though part of the nickel sites were covered. For DRM at 700 °C and 800 °C, the Ni/Al_2O_3 catalyst with 5 cycles of ZrO_2 ALD showed enhanced activity and stability, compared to the Ni/Al_2O_3 catalyst without any ZrO_2 overcoating. With the increased number of ZrO_2 ALD cycles, extremely stable performance with no activity loss was achieved for the 10ZrO_2-Ni/Al_2O_3 sample during a 100-h test at 600 °C, whereas the pristine Ni/Al_2O_3 lost a relative 59% activity. Less carbon deposition, especially the graphitic carbon, was achieved for the ZrO_2-overcoated Ni/Al_2O_3 catalysts due to the ability of ZrO_2 in CO_2 activation of surface oxygen sites.

Declaration of Competing Interest

The authors declare that they have no known competing financial interests or personal relationships that could have appeared to influence the work reported in this paper.

Acknowledgments

This work was supported in part by the U.S. Department of Energy (contract number DE-FE0029760) and Linda and Bipin Doshi endowment of Missouri University of Science and Technology. The authors would like to thank Kaiying Wang at Missouri University of Science and Technology for the help with Raman analysis. Use of the Center for Nanoscale Materials, an Office of Science user facility, was supported by the U.S. Department of Energy, Office of Science, Office of Basic Energy Sciences, under contract number DE-AC02-06CH11357.

Appendix A. Supplementary data

Supplementary data to this article can be found online at https://doi.org/10.1016/j.cej.2022.135195.

References

[1] Y. Song, E. Ozdemir, S. Ramesh, A. Adishev, S. Subramanian, A. Harale, M. Albuali, B.A. Fadhel, A. Jamal, D. Moon, S.H. Choi, C.T. Yavuz, Dry reforming of methane by stable Ni–Mo nanocatalysts on single-crystalline MgO, Science 367 (6479) (2020) 777–781.

[2] K. Li, C. Pei, X. Li, S. Chen, X. Zhang, R. Liu, J. Gong, Dry reforming of methane over $La_2O_2CO_3$-modified Ni/Al_2O_3 catalysts with moderate metal support interaction, Appl. Catal., B 264 (2020) 118448, https://doi.org/10.1016/j.apcatb.2019.118448.

[3] Y.-X. Pan, P. Kuai, Y. Liu, Q. Ge, C.-J. Liu, Promotion effects of Ga_2O_3 on CO_2 adsorption and conversion over a SiO_2-supported Ni catalyst, Energy Environ. Sci. 3 (9) (2010) 1322, https://doi.org/10.1039/c0ee00149j.

[4] M. Zhang, J. Zhang, Z. Zhou, S. Chen, T. Zhang, F. Song, Q. Zhang, N. Tsubaki, Y. Tan, Y. Han, Effects of the surface adsorbed oxygen species tuned by rare-earth metal doping on dry reforming of methane over Ni/ZrO_2 catalyst, Appl. Catal., B 264 (2020) 118522, https://doi.org/10.1016/j.apcatb.2019.118522.

[5] S. Kattel, P. Liu, J.G. Chen, Tuning selectivity of CO_2 hydrogenation reactions at the metal/oxide interface, J. Am. Chem. Soc. 139 (29) (2017) 9739–9754.

[6] Y.u. Lou, M. Steib, Q.i. Zhang, K. Tiefenbacher, A. Horváth, A. Jentys, Y. Liu, J. A. Lercher, Design of stable Ni/ZrO_2 catalysts for dry reforming of methane, J. Catal. 356 (2017) 147–156.

[7] I. Ro, J. Resasco, P. Christopher, Approaches for understanding and controlling interfacial effects in oxide-supported metal catalysts, ACS. Catal. 8 (8) (2018) 7368–7387.

[8] B. Jin, Z. Shang, S. Li, Y.-B. Jiang, X. Gu, X. Liang, Reforming of methane with carbon dioxide over cerium oxide promoted nickel nanoparticles deposited on 4-channel hollow fibers by atomic layer deposition, Catal, Sci. Technol. 10 (10) (2020) 3212–3222.

[9] B. Jin, S. Li, X. Liang, Enhanced activity and stability of MgO-promoted Ni/Al_2O_3 catalyst for dry reforming of methane: Role of MgO, Fuel 284 (2021) 119082, https://doi.org/10.1016/j.fuel.2020.119082.

[10] V. Shanmugam, R. Zapf, S. Neuberg, V. Hessel, G. Kolb, Effect of ceria and zirconia promotors on Ni/SBA-15 catalysts for coking and sintering resistant steam reforming of propylene glycol in microreactors, Appl. Catal., B 203 (2017) 859–869.

[11] J. Niu, S.E. Liland, J. Yang, K.R. Rout, J. Ran, D. Chen, Effect of oxide additives on the hydrotalcite derived Ni catalysts for CO_2 reforming of methane, Chem. Eng. J. 377 (2019), 119763.

[12] Y. Zhang, Y. Zhao, T. Otroshchenko, A. Perechodjuk, V.A. Kondratenko, S. Bartling, U. Rodemerck, D. Linke, H. Jiao, G. Jiang, Structure–activity–selectivity relationships in propane dehydrogenation over Rh/ZrO_2 catalysts, ACS. Catal. 10 (2020) 6377–6388.

[13] T. Otroshchenko, S. Sokolov, M. Stoyanova, V.A. Kondratenko, U. Rodemerck, D. Linke, E.V. Kondratenko, ZrO_2-based alternatives to conventional propane dehydrogenation catalysts: Active sites, design, and performance, Angew. Chem. Int. Ed. 54 (52) (2015) 15880–15883.

[14] M. Zhang, J. Zhang, Y. Wu, J. Pan, Q. Zhang, Y. Tan, Y. Han, Insight into the effects of the oxygen species over Ni/ZrO_2 catalyst surface on methane reforming with carbon dioxide, Appl. Catal., B 244 (2019) 427–437.

[15] F. Wang, B. Han, L. Zhang, L. Xu, H. Yu, W. Shi, CO_2 reforming with methane over small-sized Ni@ SiO_2 catalysts with unique features of sintering-free and low carbon, Appl. Catal., B 235 (2018) 26–35.

[16] Z. Li, Z. Wang, S. Kawi, Sintering and coke resistant core/yolk shell catalyst for hydrocarbon reforming, ChemCatChem 11 (2019) 202–224.

[17] H. Ge, B. Zhang, X. Gu, H. Liang, H. Yang, Z. Gao, J. Wang, Y. Qin, A tandem catalyst with multiple metal oxide interfaces produced by atomic layer deposition, Angew. Chem. Int. Ed. 55 (2016) 7081–7085.

[18] H. Yan, K. He, I.A. Samek, D. Jing, M.G. Nanda, P.C. Stair, J.M. Notestein, Tandem In_2O_3-Pt/Al_2O_3 catalyst for coupling of propane dehydrogenation to selective H_2 combustion, Science 371 (2021) 1257–1260.

[19] E. Yang, E. Nam, J. Lee, H. Lee, E.D. Park, H. Lim, K. An, Al_2O_3-coated Ni/CeO_2 nanoparticles as coke-resistant catalyst for dry reforming of methane, Catal, Sci. Technol. 10 (2020) 8283–8294.

[20] P. Littlewood, S. Liu, E. Weitz, T.J. Marks, P.C. Stair, Ni-alumina dry reforming catalysts: Atomic layer deposition and the issue of Ni aluminate, Catal. Today. 343 (2020) 18–25.

[21] Z. Shang, S. Li, L. Li, G. Liu, X. Liang, Highly active and stable alumina supported nickel nanoparticle catalysts for dry reforming of methane, Appl. Catal., B 201 (2017) 302–309.

[22] Z. Shang, S. Li, Q. Wang, X. Gu, X. Liang, Nano-engineered nickel catalysts supported on 4-channel α-Al_2O_3 hollow fibers for dry reforming of methane, AIChE. J 64 (2018) 2625–2631.

[23] Y. Zhao, Y. Kang, H. Li, H. Li, CO_2 conversion to synthesis gas via DRM on the durable Al_2O_3/Ni/Al_2O_3 sandwich catalyst with high activity and stability, Green Chem. 20 (2018) 2781–2787.

[24] S. Afzal, A.V. Prakash, P. Littlewood, T.J. Marks, E. Weitz, P.C. Stair, N.O. Elbashir, Controlling the rate of change of Ni dispersion in commercial catalyst by ALD overcoat during dry reforming of methane, Int. J. Hydrog. Energy 45 (2020) 12835–12848.

[25] P. Ingale, C. Guan, R. Kraehnert, R.N. d'Alnoncourt, A. Thomas, F. Rosowski, Design of an active and stable catalyst for dry reforming of methane via molecular layer deposition, Catal. Today. 362 (2021) 47–54.

[26] T.D. Gould, A. Izar, A.W. Weimer, J.L. Falconer, J.W. Medlin, Stabilizing Ni catalysts by molecular layer deposition for harsh, dry reforming conditions, ACS. Catal. 4 (8) (2014) 2714–2717.

[27] X. Liang, L.F. Hakim, G.-D. Zhan, J.A. McCormick, S.M. George, A.W. Weimer, J. A. Spencer, K.J. Buechler, J. Blackson, C.J. Wood, J.R. Dorgan, Novel processing to produce polymer/ceramic nanocomposites by atomic layer deposition, J. Am. Ceram. Soc. 90 (1) (2007) 57–63.

[28] D.E. Mears, Tests for transport limitations in experimental catalytic reactors, Ind. Eng. Chem. Process. Des. Dev. 10 (4) (1971) 541–547.

[29] P. Weisz, C. Prater, Interpretation of measurements in experimental catalysis, Adv. Catal., Elsevier (1954) 143–196.

[30] E. Bonera, G. Scarel, M. Fanciulli, Structure evolution of atomic layer deposition grown ZrO_2 films by deep-ultra-violet Raman and far-infrared spectroscopies, J. Non-Cryst. Solids 322 (1-3) (2003) 105–110.

[31] K. Kukli, M. Ritala, J. Aarik, T. Uustare, M. Leskelä, Influence of growth temperature on properties of zirconium dioxide films grown by atomic layer deposition, J. Appl. Phys. 92 (4) (2002) 1833–1840.

[32] J. Lu, B. Fu, M.C. Kung, G. Xiao, J.W. Elam, H.H. Kung, P.C. Stair, Coking-and sintering-resistant palladium catalysts achieved through atomic layer deposition, Science 335 (6073) (2012) 1205–1208.

[33] T.M. Onn, S. Zhang, L. Arroyo-Ramirez, Y.-C. Chung, G.W. Graham, X. Pan, R. J. Gorte, Improved thermal stability and methane-oxidation activity of Pd/Al_2O_3 catalysts by atomic layer deposition of ZrO_2, ACS. Catal. 5 (10) (2015) 5696–5701.

[34] R. Yang, C. Xing, C. Lv, L. Shi, N. Tsubaki, Promotional effect of La_2O_3 and CeO_2 on Ni/γ-Al_2O_3 catalysts for CO_2 reforming of CH_4, Appl. Catal., A 385 (1-2) (2010) 92–100.

[35] R.-P. Ye, Q. Li, W. Gong, T. Wang, J.J. Razink, L. Lin, Y.-Y. Qin, Z. Zhou, H. Adidharma, J. Tang, A.G. Russell, M. Fan, Y.-G. Yao, High-performance of nanostructured Ni/CeO_2 catalyst on CO_2 methanation, Appl. Catal., B 268 (2020) 118474, https://doi.org/10.1016/j.apcatb.2019.118474.

[36] W. Li, Y. Liu, M. Mu, F. Ding, Z. Liu, X. Guo, C. Song, Organic acid-assisted preparation of highly dispersed Co/ZrO_2 catalysts with superior activity for CO_2 methanation, Appl. Catal., B 254 (2019) 531–540.

[37] C. Rameshan, H. Li, K. Anic, M. Roiaz, V. Pramhaas, R. Rameshan, R. Blume, M. Hävecker, J. Knudsen, A. Knop-Gericke, In situ NAP-XPS spectroscopy during

methane dry reforming on ZrO_2/Pt (111) inverse model catalyst, J. Condens. Matter Phys. 30 (2018), 264007.
[38] K. Anic, A. Wolfbeisser, H. Li, C. Rameshan, K. Föttinger, J. Bernardi, G. Rupprechter, Surface spectroscopy on UHV-grown and technological Ni–ZrO_2 reforming catalysts: From UHV to Operando conditions, Top. Catal. 59 (2016) 1614–1627.
[39] H. Li, J.-I.-J. Choi, W. Mayr-Schmölzer, C. Weilach, C. Rameshan, F. Mittendorfer, J. Redinger, M. Schmid, G.N. Rupprechter, Growth of an ultrathin zirconia film on Pt_3Zr examined by high-resolution X-ray photoelectron spectroscopy, temperature-programmed desorption, scanning tunneling microscopy, and density functional theory, J. Phys. Chem. C 119 (2015) 2462–2470.
[40] A.R. Puigdollers, P. Schlexer, S. Tosoni, G. Pacchioni, Increasing oxide reducibility: The role of metal/oxide interfaces in the formation of oxygen vacancies, ACS. Catal. 7 (2017) 6493–6513.
[41] A.R. Puigdollers, G. Pacchioni, Reducibility of ZrO_2/Pt_3Zr and ZrO_2/Pt 2D films compared to bulk zirconia: A DFT+ U study of oxygen removal and H_2 adsorption, Nanoscale 9 (2017) 6866–6876.
[42] X. Jia, X. Zhang, N. Rui, X. Hu, C.-J. Liu, Structural effect of Ni/ZrO_2 catalyst on CO_2 methanation with enhanced activity, Appl. Catal., B 244 (2019) 159–169.
[43] M. Zhu, P. Tian, X. Cao, J. Chen, T. Pu, B. Shi, J. Xu, J. Moon, Z. Wu, Y.-F. Han, Vacancy engineering of the nickel-based catalysts for enhanced CO_2 methanation, Appl. Catal., B 282 (2021), 119561.
[44] L. Foppa, T. Margossian, S.M. Kim, C. Müller, C. Copéret, K. Larmier, A. Comas-Vives, Contrasting the role of Ni/Al_2O_3 interfaces in water–gas shift and dry reforming of methane, J. Am. Chem. Soc. 139 (2017) 17128–17139.
[45] J. Ni, W. Leng, J. Mao, J. Wang, J. Lin, D. Jiang, X. Li, Tuning electron density of metal nickel by support defects in Ni/ZrO_2 for selective hydrogenation of fatty acids to alkanes and alcohols, Appl. Catal., B 253 (2019) 170–178.
[46] W. Chen, G. Zhao, Q. Xue, L. Chen, Y. Lu, High carbon-resistance Ni/$CeAlO_3$-Al_2O_3 catalyst for CH_4/CO_2 reforming, Appl. Catal., B 136-137 (2013) 260–268.
[47] S. Das, J. Ashok, Z. Bian, N. Dewangan, M.H. Wai, Y. Du, A. Borgna, K. Hidajat, S. Kawi, Silica-ceria sandwiched Ni core–shell catalyst for low temperature dry reforming of biogas: Coke resistance and mechanistic insights, Appl. Catal., B 230 (2018) 220–236.
[48] P. Ferreira-Aparicio, A. Guerrero-Ruiz, I. Rodríguez-Ramos, Comparative study at low and medium reaction temperatures of syngas production by methane reforming with carbon dioxide over silica and alumina supported catalysts, Appl. Catal., A 170 (1) (1998) 177–187.
[49] J.-W. Kim, J.-A. Ha, H. Jung, B.-II. Ahn, S.-H. Lee, J.-G. Choi, Kinetic analysis of supported Ni-catalyzed CO_2/CH_4 reactions using photoacoustic spectroscopy, Phys. Chem. Chem. Phys. 9 (43) (2007) 5828, https://doi.org/10.1039/b709102h.
[50] L. Karam, M. Armandi, S. Casale, V. El Khoury, B. Bonelli, P. Massiani, N. El Hassan, Comprehensive study on the effect of magnesium loading over nickel-ordered mesoporous alumina for dry reforming of methane, Energy Convers. Manag. 225 (2020) 113470, https://doi.org/10.1016/j.enconman.2020.113470.
[51] S. Kim, B.S. Crandall, M.J. Lance, N. Cordonnier, J. Lauterbach, E. Sasmaz, Activity and stability of NiCe@ SiO_2 multi–yolk–shell nanotube catalyst for tri-reforming of methane, Appl. Catal., B 259 (2019), 118037.
[52] L.-Y. Shi, Y.-X. Li, D.-M. Xue, P. Tan, Y. Jiang, X.-Q. Liu, L.-B. Sun, Fabrication of highly dispersed nickel in nanoconfined spaces of as-made SBA-15 for dry reforming of methane with carbon dioxide, Chem. Eng. J. 390 (2020), 124491.